Full length article

Bone structure and composition in a hyperglycemic, obese, and leptin receptor-deficient rat: Microscale characterization of femur and calvarium

Chiara Micheletti [a,b], Martina Jolic [b], Kathryn Grandfield [a,c,d], Furqan A. Shah [b], Anders Palmquist [b,*]

[a] *Department of Materials Science and Engineering, McMaster University, Hamilton, ON, Canada*
[b] *Department of Biomaterials, Sahlgrenska Academy, University of Gothenburg, Gothenburg, Sweden*
[c] *School of Biomedical Engineering, McMaster University, Hamilton, ON, Canada*
[d] *Brockhouse Institute for Materials Research, McMaster University, Hamilton, ON, Canada*

ARTICLE INFO

ABSTRACT

Metabolic abnormalities, such as diabetes mellitus and obesity, can impact bone quantity and/or bone quality. In this work, we characterize bone material properties, in terms of structure and composition, in a novel rat model with congenic leptin receptor (LepR) deficiency, severe obesity, and hyperglycemia (type 2 diabetes-like condition). Femurs and calvaria (parietal region) from 20-week-old male rats are examined to probe bones formed both by endochondral and intramembranous ossification. Compared to the healthy controls, the LepR-deficient animals display significant alterations in femur microarchitecture and in calvarium morphology when analyzed by micro-computed X-ray tomography (micro-CT). In particular, shorter femurs with reduced bone volume, combined with thinner parietal bones and shorter sagittal suture, point towards a delay in the skeletal development of the LepR-deficient rodents. On the other hand, LepR-deficient animals and healthy controls display analogous bone matrix composition, which is assessed in terms of tissue mineral density by micro-CT, degree of mineralization by quantitative backscattered electron imaging, and various metrics extrapolated from Raman hyperspectral images. Some specific microstructural features, i.e., mineralized cartilage islands in the femurs and hyper-mineralized areas in the parietal bones, also show comparable distribution and characteristics in both groups. Overall, the altered bone microarchitecture in the LepR-deficient animals indicates compromised bone quality, despite the normal bone matrix composition. The delayed development is also consistent with observations in humans with congenic Lep/LepR deficiency, making this animal model a suitable candidate for translational research.

1. Introduction

Skeletal development generally proceeds via either endochondral or intramembranous ossification [1–3]. The primary difference between these two main ossification mechanisms is whether bone formation is preceded by a cartilaginous intermediate, as in endochondral ossification, or not, as in intramembranous ossification where tissue is laid down directly as bone. Bones serve essential functions to provide the structural framework for the body, protect internal organs, assist locomotion, maintain mineral homeostasis, and support blood cell production [1]. Bone tissue is also an exquisite material, at the same time tough and strong thanks to the hierarchical organization of its components [4].

Bone strength, and in turn its mechanical and biological functioning,

relies not only on bone mineral density (BMD), a metric related to bone mass, i.e., bone *quantity*, but also on bone *quality*, defined as the "totality of features and characteristics that influence a bone's ability to resist fracture" [5], encompassing its material properties (structure and composition). Aging and disease can compromise bone quantity and/or quality, leading to an increased fracture risk [6,7]. For example, metabolic changes induced by type 2 diabetes mellitus (T2DM) and often concurrent obesity also affect bone metabolism and remodeling [8–10]. As a consequence, despite normal or even higher BMD than in the healthy population, diabetic subjects have an increased fracture risk as a result of poor bone quality [11,12].

Different mechanisms have been proposed to explain the altered bone quality in T2DM and obesity. Bone fragility in diabetic subjects has

---

often been correlated with the accumulation of advanced glycation end-products (AGEs), both crosslinked, such as pentosidine (PEN), and non-crosslinked, such as carboxymethyl lysine (CML) [13]. Non-enzymatic crosslinking induced by AGEs such as PEN has been associated with an increased brittleness of collagen fibers, likely causing loss in bone strength [14]. It also appears that fat accumulation in hyperglycemic conditions and obesity promotes the differentiation of mesenchymal stem cells in adipocytes rather than osteoblasts, in turn favouring adipogenesis over osteoblastogenesis [10,11]. While the effect of T2DM on osteoclasts remains unclear, osteoclastic activity could be overall stimulated through the RANKL/RANK/OPG pathway due to the increased production of inflammatory cytokines [15].

Animal models to study T2DM are often diet-induced or monogenic/polygenic models of obesity. Monogenic models are mostly based on mutations of the gene encoding leptin (Lep) or of the leptin receptor (LepR) [16]. Leptin, a cytokine-like hormone mainly produced by adipocytes, plays an important role in regulating energy storage and appetite [17]. Several studies have documented that mutations in Lep and LepR impacts bone metabolism, but the underlying mechanisms are still unclear, and contrasting outcomes in terms of bone mass have been observed [18]. Leptin is mediated both by the central nervous system and the sympathetic nervous system, hence skeletal changes are due to the overall balance between central and peripheral mechanisms of action [18]. Leptin has also direct effects on bone cells, as they have a leptin receptor [19]. Reduced bone length and/or mass have been commonly reported in the appendicular skeleton [20–22], while an increased trabecular bone volume is often observed in the spine of Lep/LepR-deficient rodents [23,24]. While some investigators have postulated that leptin is bone anabolic through the peripheral pathway, but catabolic through the central one [25], others have found that central (intracerebroventricular) administration of leptin promotes bone growth [26].

There exist concerns on the translation of Lep/LepR-deficient animal models to diabetes research in humans due to the dissimilar disease etiology [27]. However, it is worth pointing out that congenic Lep/LepR deficiency has been reported, although rarely, also in humans, where it manifests with severe obesity already during childhood [28–31]. The rarity of this condition has impacted bone research in Lep/LepR-deficient human subjects. A clear bone phenotype has not been identified yet, and systemic leptin administration leads to both unchanged and increased BMD in the few studies available [18].

In this work, we examine bone structure and composition in a congenic LepR-deficient rat, the Lund MetS (metabolic syndrome) rat, that displays obesity and hyperglycemia, as well as micro- and macro-vascular changes typical of diabetes [32–34]. To our knowledge, this is the first study evaluating the skeleton of this rodent as a potential candidate animal model for LepR deficiency and T2DM-like conditions in bone research. Multiscale characterization was performed on bone tissue from the femur and calvarium (parietal bones and sagittal suture) to probe formation by endochondral and intramembranous ossification, respectively. Bone morphology and microarchitecture were investigated with micro-computed X-ray tomography (micro-CT) and scanning electron microscopy (SEM). Bone mineralization was evaluated as tissue mineral density (TMD) by micro-CT and as BMD distribution (BMDD) by quantitative backscattered electron imaging (qBEI). Bone matrix composition, in terms of degree of mineralization, carbonate substitution, and mineral crystallinity/maturity, was assessed by Raman hyperspectral imaging. Mechanical properties of the femurs were measured by reference point indentation (RPI). Our analyses also probed site-specific microstructural features, including mineralized cartilage islands in the femurs and bands of increased mineral content in the calvaria.

2. Materials and methods

2.1. Animal study, sample retrieval and preparation

Two variants of the male Lund MetS rat, a congenic (Cg) rat with a LepR mutation introduced on a BioBreeding Diabetes Resistant Rat (BBDR) [32], were obtained from Janvier Labs (France) [35]: i) BBDR. Cg-LepR$^{+/+}$ (abbreviated to LepR$^{+/+}$ hereinafter), lean and with normal insulin sensitivity (euglycemia) ($n = 10$); ii) BBDR.Cg-LepR$^{-/-}$ (abbreviated to LepR$^{-/-}$ hereinafter), LepR-deficient, severely obese and with insulin resistance (hyperglycemia) ($n = 11$). The study was approved by the Animal Research Ethics Committee of Gothenburg (Dnr. 14790/2019). At both 16 and 20 weeks of age, LepR$^{-/-}$ animals had a greater weight and blood glucose level than LepR$^{+/+}$ animals ($p < 0.001$) (Tables 1, S1). High blood glucose in the LepR$^{-/-}$ group confirms their hyperglycemic condition (Tables 1, S1). At 20 weeks of age, animals were sacrificed. Their femurs (left and right) and calvaria were retrieved and fixed in 10% neutral buffered formalin. Femur length was measured with a caliper. Micro-CT was performed on unembedded samples, while SEM and micro-Raman spectroscopy were carried out post-resin embedding, as described below.

Femurs. After micro-CT, right femurs were sectioned transversally (with respect to the long axis of the femur) to separate the femur head from the distal to mid-diaphysis portion. The distal to mid-diaphysis portions were sectioned longitudinally (with respect to the long axis of the femur), dehydrated in ethanol and resin embedded (LR White, London Resin Co. Ltd., UK). After embedding, samples were polished with SiC paper (800, 1200, 2000, and 4000 grit; ISO grit designation). Only the half towards the medial side was considered for qBEI and micro-Raman spectroscopy.

Calvaria. After micro-CT, calvaria were dehydrated in ethanol, resin embedded (LR White, London Resin Co. Ltd., UK), and cross-sectioned along the coronal plane in the parietal bone region, approximately at one third of the length of the sagittal suture towards the frontal bone side. Samples were polished with SiC paper (800, 1200, 2000, and 4000 grit; ISO grit designation).

2.2. Micro-CT

For both femurs and calvaria, micro-CT data were acquired with a SkyScan 1172 (Bruker, MA, USA), reconstructed in NRecon (Bruker, Billerica, USA), aligned in DataViewer (Bruker, MA, USA), and visualized and analyzed in Dragonfly 2020.2 (Objects Research Systems, QC, Canada). Standards of hydroxyapatite (⌀ = 2 mm) with known density (0.25 and 0.75 g/cm^3) were used to obtain a calibration line to convert the pixel intensity in micro-CT data into TMD (expressed in g/cm^3) [36].

Femurs. Right and left femurs ($n = 8$/group) were scanned with a 70 kV X-ray beam, Al—Cu filter, 180° rotation range, 0.7° step size, 3 frame averaging, and 13.90 μm pixel size. Morphometry metrics were measured in three dimensions (3D) using the "Bone Analysis" plug-in in Dragonfly 2020.2 (Objects Research Systems, QC, Canada), segmenting trabecular and cortical bone with the Buie algorithm (input guess for trabecular thickness = 125 μm) [37]. For trabecular bone, morphometry parameters (bone volume fraction, BV/TV; trabecular thickness, Tb.Th;

Table 1

Values of weight and blood glucose measured at 16 and 20 weeks of age.

Group	Weight at 16 weeks [g]	Weight at 20 weeks [g]	Blood glucose at 16 weeks [mmol/l]	Blood glucose at 20 weeks [mmol/l]
LepR$^{+/+}$	381 ± 27	422 ± 21	9.7 ± 1.0	9.4 ± 1.5
LepR$^{-/-}$	553 ± 41***	598 ± 48***	24.1 ± 6.6***	24.9 ± 5.0***

*** Denotes statistical significance with respect to the control group ($p < 0.001$).

trabecular separation, Tb.Sp) were evaluated in the distal femur metaphysis, selecting a region with a height equal to 5% of the average femur length in each group (i.e., 1.946 and 1.723 mm in LepR^{+/+} and LepR^{-/-}, respectively), at a consistent distance from the growth plate (Fig. S1). Trabecular number (Tb.N) was computed as the reciprocal of the sum of Tb.Th and Tb.Sp (following the guidelines of Skyscan CT-analyser). For cortical bone, morphometry parameters (cortical thickness, Ct.Th; cortical bone area, Ct.Ar; total cross-sectional area inside the periosteal envelope, Tt.Ar; cortical area fraction, Ct.Ar/Tt.Ar) were measured in the femur diaphysis, selecting a region with a height equal to 5% of the average femur length in each group (i.e., with the same height as the region used for trabecular bone analysis) at a consistent distance from the growth plate (Fig. S1). The proximal portion of right and left femurs ($n = 8$/group) was scanned with a 70 kV X-ray beam, Al—Cu filter, 180° rotation range, 0.7° step size, 3 frame averaging, and 26.72 µm pixel size. Morphology of the femoral head and neck was evaluated qualitatively in Dragonfly 2020.2 (Objects Research Systems, QC, Canada).

Calvaria. Calvaria ($n = 8$/group) were scanned with a 49 kV X-ray beam, Al filter, 360° rotation range, 0.7° step size, 5 frame averaging, and 17.90 µm pixel size. Parietal bone thickness was evaluated in a region 285×335 px^2 in the axial plane (xy plane), centred at mid-length of the sagittal suture and encompassing the entire calvaria thickness (z direction). In this region, parietal bones were separated from non-bone regions by Otsu thresholding. The sagittal suture was examined using the same region used to examine the parietal bones, but limiting the analyses to 25 px-thick region approximately centred in the mid-point of the calvaria thickness. In this region, the sagittal suture was segmented by Otsu thresholding, followed by a "Process island" operation to remove noise, and manual refinement to remove mis-labelled regions. Parietal bone thickness and sagittal suture width were measured with the "Volume thickness map" operation, taking the average value in the distribution of thickness measurements. Variation in suture length (in the xy plane) along the calvaria thickness (z direction) was evaluated with the "Slice analysis" module by computing the perimeter ($2p$) and thickness (t) of the ROI corresponding to the segmented suture in each xy slice, and estimating the length (l) by subtracting the thickness from the semi-perimeter ($l = p - t$).

2.3. SEM and qBEI

Embedded samples were imaged in backscattered electron (BSE) mode in a Quanta 200 environmental SEM (FEI Company, The Netherlands) operated at 20 kV in low vacuum mode (1 Torr water vapour pressure), with a working distance of 10 mm. For qBEI analyses ($n = 3$/group), image calibration and acquisition were completed following published protocols [38], using a custom-made standard of pure C and pure Al. Briefly, for each imaging session (i.e., for each sample), standard and sample were loaded in the instrument at the same time. Brightness and contrast in BSE-SEM images were adjusted to have an average grey-level of 25 and 225 in the C and Al regions of the standard, respectively [38]. After this calibration, BSE-SEM images of the sample were acquired in a mosaic fashion, and combined into an overview image manually in Photoshop (Adobe, CA, USA) without altering their grey-levels. The overview mosaic images were processed in Python 3.8.10 to convert grey-levels into wt% Ca content. Regions of bone and resin were separated by Otsu thresholding using the "threshold_otsu" module in the "skimage.filters" library. The x-axis of the greyscale histogram of the bone region (upper range of Otsu thresholding) was converted in wt% Ca using pure hydroxyapatite (39.86 wt% Ca) [38] and the C standard [39] as reference points for 39.86 wt% Ca and 0.17 wt% Ca, respectively. The grey-level of these two reference points was computed from the grey-level/atomic number (Z) calibration line [38], obtained by averaging the mean grey-level in the C ($Z = 6$) and Al ($Z = 12$) regions for each imaging session. Following established protocols [38], BMDD was evaluated in terms of weighted mean Ca concentration (Ca-Mean), peak height of the distribution (MaxFreq),

peak position of the most frequent Ca concentration (Ca-MaxFreq), full-width half maximum (FWHM), spread of the distribution on the low concentration side (SpLow), and spread of the distribution on the high concentration side (SpHigh). Frequency values below 0.001% were excluded from BMDD analysis. FWHM was obtained using the "find_peaks" and "peak_widths" functions in the "scipy.signal" library. SpLow and SpHigh were evaluated by comparing the acquired histogram to an equivalent-area Gaussian curve [38], computing their integral areas with the composite trapezoidal rule using the "numpy.trapz" function. Lastly, the range 10–30 wt% Ca was divided in bins with a width equal to 5 wt% Ca, and the number of pixels in each bin was counted and normalized by the total number of pixels in the 10–30 wt% Ca range.

2.4. Micro-Raman spectroscopy

Micro-Raman spectroscopy was performed in a Renishaw inVia Qontor (Renishaw PLC, UK) equipped with a 633 nm laser and Live-Track focus-tracking technology. The laser was focused on the surface using a $\times 100$ (0.9 NA) objective. Raman signal was collected using a Peltier cooled CCD deep depletion NIR enhanced detector behind a 1800 g mm^{-1} grating (1.0 ± 0.15 cm^{-1} step size). Spectra were baseline subtracted (intelligent spline fitting with 10 nodes and 1.3 noise level), cleaned of cosmic rays, and denoised by Principal Component Analysis (PCA) with a component auto-correlation limit of 0.7 (default value) in Renishaw WiRE 5.4 (Renishaw PLC, UK). Spectra were analyzed in Python 3.8.10. The following Raman peaks were considered [40]: phosphate (PO_4^{3-}) ν_1 (~930–980 cm^{-1}) and ν_2 (~410–460 cm^{-1}); amide III (~1215–1300 cm^{-1}); carbonate (CO_3^{2-}) (~1050–1100 cm^{-1}); phenylalanine (Phe) (~1000–1005 cm^{-1}). Mineral-to-matrix ratio was obtained from the ratio $\nu_2PO_4^{3-}$/amide III [40] and the ratio $\nu_1PO_4^{3-}$/Phe [41]. Carbonate-to-phosphate ratio was obtained from the ratio $CO_3^{2-}/\nu_2PO_4^{3-}$ [40]. For all these ratios, integral peak areas were computed with the composite trapezoidal rule using the "numpy.trapz" function. Mineral crystallinity was evaluated as the reciprocal of the FWHM of the $\nu_1PO_4^{3-}$ peak [42], which was computed using the "find_peaks" and "peak_widths" functions in the "scipy.signal" library, after Voigt-fitting of the $\nu_1PO_4^{3-}$ peak using the "curve_fit" function in the "scipy.optimize" library.

2.4.1. Femurs

Maps were acquired with a pixel size of 10 µm, 1 s exposure, and 2 accumulations in both cortical and trabecular bone in 65×95 px^2 and 70×60 px^2 areas, respectively ($n = 3$/group). When analyzing these maps, resin regions were excluded by setting a threshold at 40% of the $\nu_1PO_4^{3-}$ peak intensity. High-resolution maps with a pixel size of 1 µm were acquired with 1 s exposure and 2 accumulations in specific 50×100 µm^2 ROIs in both cortical and trabecular femoral bone, specifically on areas containing bone-mineralized cartilage interfaces ($n = 3$/group). Areas of bone and mineralized cartilage in the Raman maps of the $\nu_1PO_4^{3-}$ peak intensity were segmented using the "Kmeans" function in the "sklearn.cluster" library (4 clusters) in Python 3.8.10. Only data points in the 5% to 95% quantiles of the $\nu_1PO_4^{3-}$ peak intensity were considered for segmentation and analysis.

2.4.2. Calvaria

Maps were acquired with a pixel size of 10 µm, 1 s exposure, and 2 accumulations in $80–90 \times 70–85$ px^2 areas in the parietal bone in proximity to the sagittal suture ($n = 3$/group). When analyzing these maps, resin regions were excluded by setting a threshold at 25% of the $\nu_1PO_4^{3-}$ peak intensity. High-resolution maps with a pixel size of 1 µm were acquired with 1 s exposure and 2 accumulations in specific 50×100 µm^2 ROIs in areas containing bone interfacing with hypermineralized bone ($n = 3$/group). Areas of bone and hyper-mineralized bone in the Raman maps of the $\nu_1PO_4^{3-}$ peak intensity were segmented using the "Kmeans" function in the "sklearn.cluster" library (5 clusters) in Python 3.8.10. Only data points in the 5% to 95% quantiles of the

$v_1PO_4^{3-}$ peak intensity were considered for segmentation and analysis.

2.5. RPI

Mechanical properties were evaluated ex vivo by RPI using a BioDent microindenter (Active Life Scientific, CA, USA) in right and left proximal femurs ($n = 6$/group). Three measurements were acquired in each sample by applying an indentation force of 4 N at a frequency of 2 Hz in 10 cycles using a 90° cono-spherical (≤ 5 µm radius point) test probe and a flat bevel reference probe. The following parameters were assessed: 1st cycle indentation distance (ID 1st); 1st cycle unloading slope (US 1st); 1st cycle creep indentation distance (CID 1st); total indentation distance (TID); indentation distance increase (IDI); average creep indentation distance (Avg CID); average energy dissipated (Avg ED); and average unloading slope (Avg US).

2.6. Statistical analysis

Statistical significance of micro-CT data was evaluated with the Student's *t*-test ($\alpha = 0.05$), after verifying normality with the Shapiro-Wilk test ($\alpha = 0.05$) and homoscedasticity with the Brown-Forsythe test ($\alpha = 0.05$). In case of homoscedasticity violation, the unequal variance correction was applied to the Student's *t*-test, i.e., a Welch's *t*-test was performed instead ($\alpha = 0.05$). Statistical significance of qBEI, micro-Raman spectroscopy, and RPI data was evaluated with the Mann-Whitney *U* test ($\alpha = 0.05$). Statistical analysis was completed in Python 3.8.10 using the "scipy.stats" library. Data are reported as mean ± standard deviation.

3. Results

3.1. Femurs

3.1.1. Structure

3D reconstructions of micro-CT scans revealed that LepR$^{-/-}$ animals presented not fully developed femoral head and neck (Figs. 1A, S2), as well as overall shorter femurs (caliper measurements) ($p < 0.001$) (Fig. 1B, Table S2). In the trabecular space, LepR$^{-/-}$ animals had thinner trabeculae (Tb.Th), although not significantly with respect to LepR$^{+/+}$ animals ($p > 0.05$), as well as lower BV/TV ($p < 0.01$), higher Tb.Sp ($p < 0.01$), and reduced Tb.N ($p < 0.05$) (Fig. 1C, Table S2). In the cortical region, the LepR$^{-/-}$ group displayed significantly smaller values of Ct.Ar, Tt.Ar, Ct.Ar/Tt.Ar, and Ct.Th ($p < 0.001$ for Ct.Ar, Tt.Ar, and Ct.Th; $p < 0.01$ for Ct.Ar/Tt.Ar) (Fig. 1C, Table S2).

3.1.2. Composition

LepR$^{+/+}$ and LepR$^{-/-}$ animals did not display statistically significant differences in TMD measured in micro-CT data in neither cortical (Ct. TMD) nor trabecular (Tb.TMD) bone ($p > 0.05$) (Table S2). Comparable composition between animal groups was also confirmed by qBEI, as there were no significant differences in any of the metrics evaluated (Ca-Mean, FWHM, MaxFreq, Ca-MaxFreq, SpLow, SpHigh) ($p > 0.05$) (Figs. 2A-B, S3, Table S3). Similarly, the number of pixels in different 5 wt% Ca-wide bins was analogous in the two groups ($p > 0.05$) (Table S4). Raman maps with 10 µm pixel size confirmed the presence of regions with higher mineral content throughout the bone matrix noted in BSE-SEM and qBEI images in both cortical and trabecular bone (Figs. 2C, S4). LepR$^{-/-}$ and LepR$^{+/+}$ animals had statistically comparable mineral-to-matrix ratio, carbonate-to-phosphate ratio, and mineral crystallinity in both cortical and trabecular bone ($p > 0.05$) (Figs. 2C, S5, Table S5),
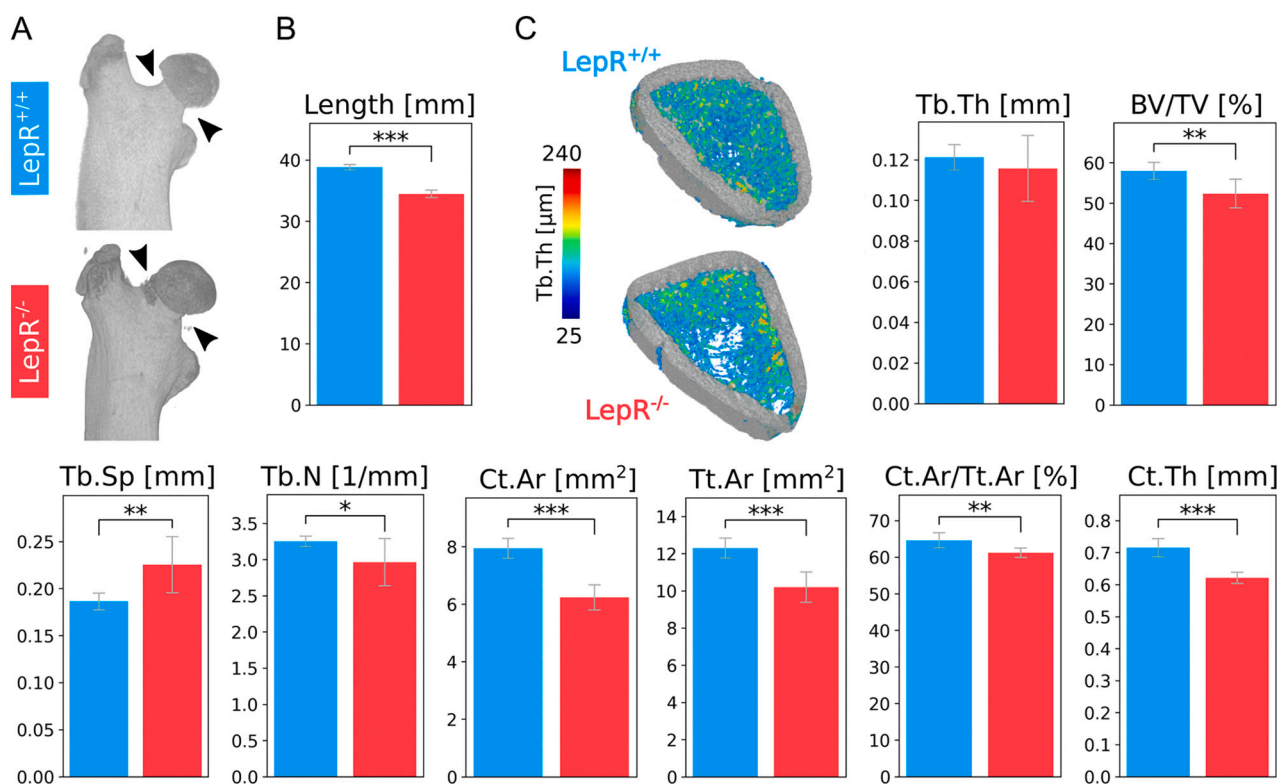

Fig. 1. Femur structure. A) 3D reconstruction of micro-CT scans of representative femur heads. Under-developed head and neck can be noted in the femur of LepR$^{-/-}$ animals (arrowheads). B) Bar plot of femur length obtained by caliper measurements, showing that the LepR$^{-/-}$ group (red bar) has significantly shorter femurs than LepR$^{+/+}$ animals (blue bar). C) 3D reconstruction of a representative femur section with volume thickness map of Tb.Th, and bar plots of morphometry parameters obtained from micro-CT scans. *, **, and *** in the bar plots denote statistical significance ($p < 0.05$, $p < 0.01$, and $p < 0.001$, respectively). (For interpretation of the references to colour in this figure legend, the reader is referred to the web version of this article.)
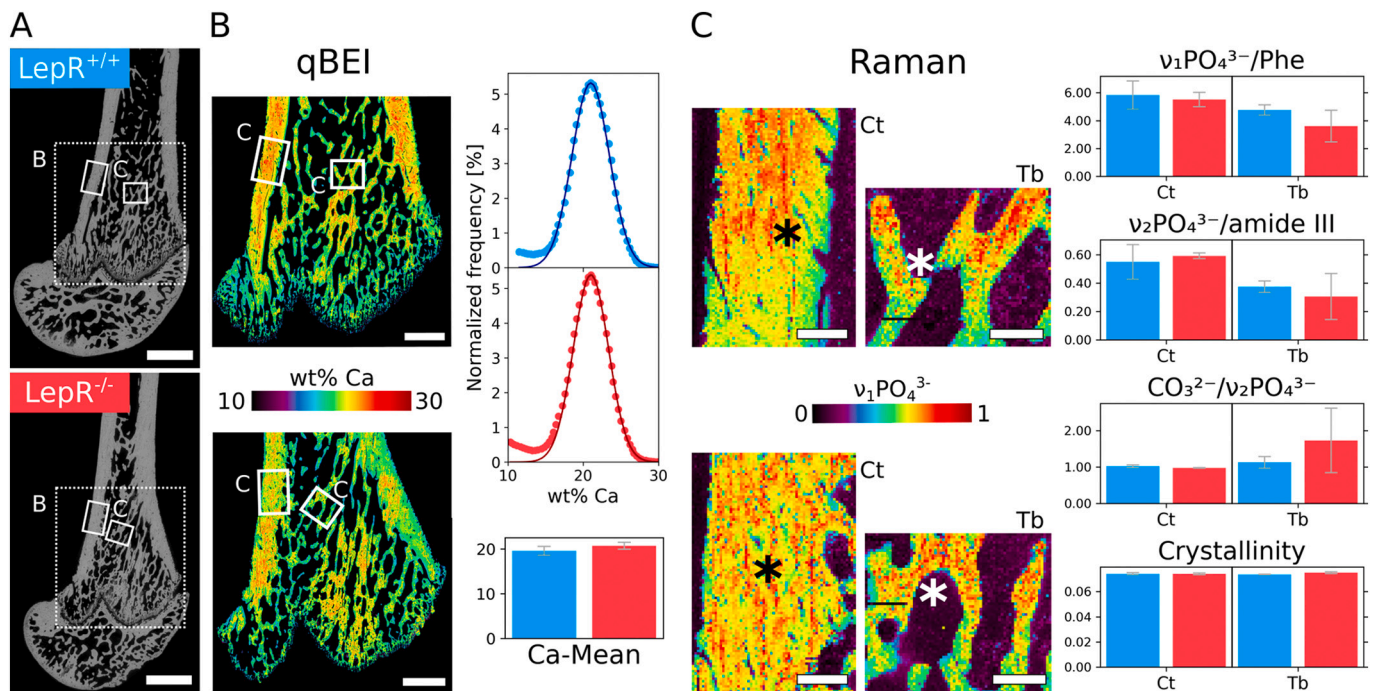
Fig. 2. Femur composition. A) Overview BSE-SEM image of longitudinal sections of a representative femur of LepR$^{+/+}$ (colour-coded in blue) and LepR$^{-/-}$ animals (colour-coded in red), with marked areas indicating the regions where qBEI (dotted border, B) and Raman (solid border, C) analyses were completed. B) qBEI images where pixel intensity corresponds to mineral concentration, expressed as wt% Ca, with corresponding histograms (dots represent the histogram of the acquired data, and continuous line corresponds to the area-equivalent Gaussian curve) and bar plot for Ca-Mean. C) Raman maps (10 μm pixel size) of the $\nu_1 PO_4^{3-}$ peak intensity (normalized by the maximum value registered in the map), and bar plots summarizing the values of mineral-to-matrix ratio ($\nu_2 PO_4^{3-}$/amide III; $\nu_1 PO_4^{3-}$/Phe), carbonate-to-phosphate ratio ($CO_3^{2-}/\nu_2 PO_4^{3-}$), and mineral crystallinity (1/FWHM) measured in the maps. In the qBEI images and Raman maps, more mineralized regions (orange-to-red) can be noted throughout the bone matrix in both cortical and trabecular bone. Some of these regions (* in the Raman maps) were examined at higher resolution (1 μm pixel size Raman maps, see Fig. 3). Scale bars are 2 mm in A, 1 mm in B, and 200 μm in C. (For interpretation of the references to colour in this figure legend, the reader is referred to the web version of this article.)

confirming TMD and qBEI observations. Although values of mineral-to-matrix ratio were higher in the LepR$^{+/+}$ animals in both femoral cortical and trabecular bone (with the exception of the ratio $\nu_2 PO_4^{3-}$/amide III in cortical bone), differences failed to reach statistical significance. No statistically significant differences in these metrics were found also when considering high-resolution Raman maps (1 μm pixel size) ($p > 0.05$) (Tables S6, S7).

3.1.3. Notable microstructural features

In BSE-SEM images, areas without osteocytes and with higher contrast than the surrounding bone matrix were observed in both cortical and trabecular regions (Fig. 3A-D). These areas are believed to correspond to islands of mineralized cartilage. High-resolution Raman maps (1 μm pixel size) of the regions where bone interfaces with mineralized cartilage islands confirmed the higher mineral content (i.e., mineral-to-matrix ratio) of mineralized cartilage compared to bone (Figs. 3E-H, S6), although the difference was not statistically significant in either group, both in cortical and trabecular regions ($p > 0.05$). Analogously, carbonate-to-phosphate ratio was higher in the mineralized cartilage islands than in bone in both groups, but not significantly ($p > 0.05$). Values of mineral crystallinity (1/FWHM) were very similar in mineralized cartilage islands and bone ($p > 0.05$) (Figs. 3I-J, S7, Tables S6, S7).

3.1.4. Mechanical properties

Mechanical properties evaluated by RPI revealed no statistically significant differences for any of the metrics assessed (Tables 2, S8).

3.2. Calvaria

3.2.1. Structure

The LepR$^{-/-}$ group displayed significantly thinner parietal bones ($p < 0.001$) than the LepR$^{+/+}$ group (Fig. 4A, Table S9). Sagittal suture was significantly narrower and shorter in the LepR$^{-/-}$ animals ($p < 0.001$ for width; $p < 0.01$ for length) (Fig. 4B, Table S9). In both groups, the suture length increased across the calvaria thickness in the direction from the dura mater side towards the cranium exterior (Fig. 4C).

3.2.2. Composition

LepR$^{+/+}$ and LepR$^{-/-}$ animals did not display statistically significant differences in TMD measured in micro-CT scans ($p > 0.05$) (Table S9). Similarly, qBEI showed no significant difference between LepR$^{-/-}$ and LepR$^{+/+}$ groups for any of the metrics evaluated (Ca-Mean, FWHM, MaxFreq, Ca-MaxFreq, SpLow, SpHigh) ($p > 0.05$) (Figs. 5A, S8, Table S10). Similarly, no differences in the number of pixels in the 5 wt% Ca-wide bins were observed between groups ($p > 0.05$) (Table S11). LepR$^{-/-}$ and LepR$^{+/+}$ animals also had comparable mineral-to-collagen ratio, carbonate-to-phosphate ratio, and mineral crystallinity in the parietal region, as evaluated from 10 μm pixel size Raman maps ($p > 0.05$) (Figs. 5B, S9, S10, Table S12). No statistically significant differences in these metrics were found also when considering high-resolution Raman maps (1 μm pixel size) ($p > 0.05$) (Table S13).

3.2.3. Notable microstructural features

Areas with an increased mineral content, approximately centrally-located in the parietal bones cross-sections, as well as close to the sagittal suture, were noted in BSE-SEM images, where contrast is composition-based, as well as in qBEI and Raman maps with 10 μm pixel size. These areas, herein labelled as hyper-mineralized bone, were better
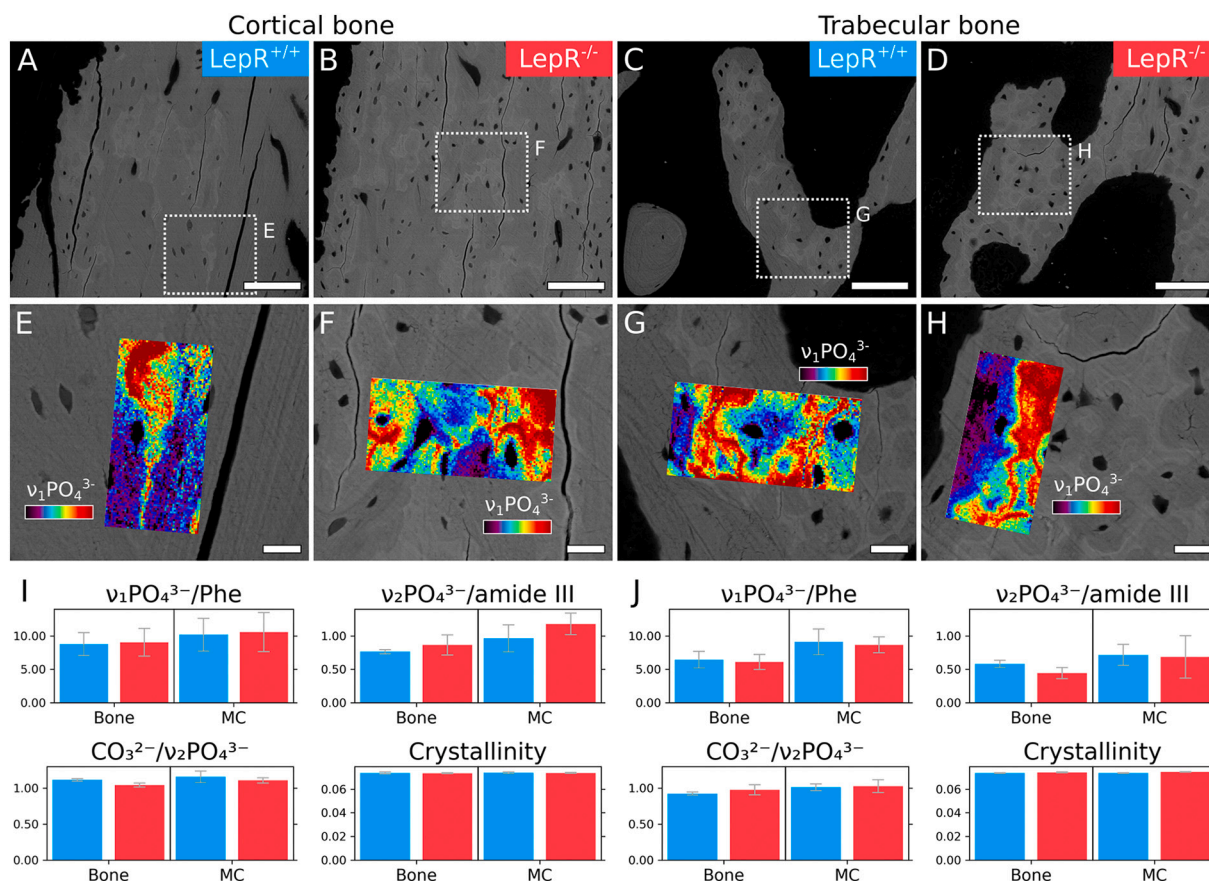
Fig. 3. Mineralized cartilage islands. A-D) Representative BSE-SEM image where mineralized cartilage islands can be distinguished as the lighter grey regions within bone matrix (dark grey) in both cortical (A, B) and trabecular bone (C, D) in both LepR$^{+/+}$ (A, C) and LepR$^{-/-}$ (B, D) animals. E-H) Higher magnification BSE-SEM images (corresponding to A-D, respectively) with superimposed Raman maps (1 μm pixel size) of the $\nu_1PO_4^{3-}$ peak intensity (restricted to 5–95% quantile range). I-J) Bar plots summarizing the values of mineral-to-matrix ratio ($\nu_2PO_4^{3-}$/amide III; $\nu_1PO_4^{3-}$/Phe), carbonate-to-phosphate ratio ($CO_3^{2-}/\nu_2PO_4^{3-}$), and mineral crystallinity (1/FWHM) measured in bone and mineralized cartilage (MC) in the Raman maps acquired in cortical and trabecular bone, respectively. Scale bars are 100 μm in A-D, and 20 μm in E-H.

Table 2
RPI measurements in the proximal femurs.

Parameter	LepR$^{+/+}$	LepR$^{-/-}$
IDI 1st [μm]	42.0 ± 4.2	40.8 ± 4.2
US 1st [N/μm]	0.334 ± 0.040	0.334 ± 0.041
CID 1st [μm]	3.94 ± 0.39	3.78 ± 0.66
TID [μm]	45.0 ± 4.4	43.7 ± 4.3
IDI [μm]	6.11 ± 0.41	5.99 ± 0.36
Avg CID [μm]	1.39 ± 0.27	1.26 ± 0.17
Avg ED [μJ]	9.6 ± 1.1	10.1 ± 1.2
Avg US [N/μm]	0.352 ± 0.047	0.353 ± 0.045

examined in high-resolution Raman maps (1 μm pixel size) (Figs. 6A-D, S11), which confirmed the higher mineral content (mineral-to-matrix ratio) of hyper-mineralized bone compared to bone, although the difference was not statistically significant in either group ($p > 0.05$). Similarly, carbonate-to-phosphate ratio was higher in hyper-mineralized bone than bone in both groups, but not significantly ($p > 0.05$). No differences in mineral crystallinity in hyper-mineralized bone and bone were noted ($p > 0.05$) (Figs. 6E, S12, Table S13).

4. Discussion

We examined the structure and composition of the femur and the calvarium (parietal region) as examples of bones formed by endochondral and intramembranous ossification, respectively, in a novel rodent model with congenic LepR deficiency, the Lund MetS rat [32,35]. Analogously to what has been reported in humans with LepR deficiency [29–31], the LepR$^{-/-}$ rats displayed severe early-onset obesity, with a greater weight than the LepR$^{+/+}$ animals (Table 1). Additionally, elevated blood glucose levels confirmed hyperglycemia (Table 1), pointing towards the co-presence of a diabetic (type 2) condition.

One of the most widespread rat models for obesity-induced T2DM is the LepR-deficient Zucker fatty (fa/fa) rat, together with its sub-strain Zucker diabetic fatty (ZDF) rat [27]. Zucker fatty rats develop obesity at 4 weeks of age [16], similarly to the Lund MetS LepR$^{-/-}$ rats used herein, which are severely obese at 30 days of age [35]. ZDF rats have increased diabetic features than Zucker fatty rats, with overt diabetes at 8–10 weeks of age, but less obesity [16]. On the other hand, Lund MetS LepR$^{-/-}$ male rats are both severely obese and develop diabetes by 145 days of age [35]. Therefore, this rat model can be a promising alternative to combine obese and diabetic characteristics. Moreover, it closely resembles traits of the metabolic syndrome in humans [35], together with diabetes-related vascular complications [32–34].

4.1. Structure

Micro-CT of femurs revealed an abnormal microarchitecture in LepR$^{-/-}$ animals in both cortical and trabecular bone, with reduced cortical and trabecular thickness, lower cortical area, and lower bone mass in the trabecular compartment, given the lower BV/TV and Tb.N, and the increased Tb.Sp. The femurs were also nearly 5 mm shorter in the LepR$^{-/-}$ group. These findings are consistent with the skeletal
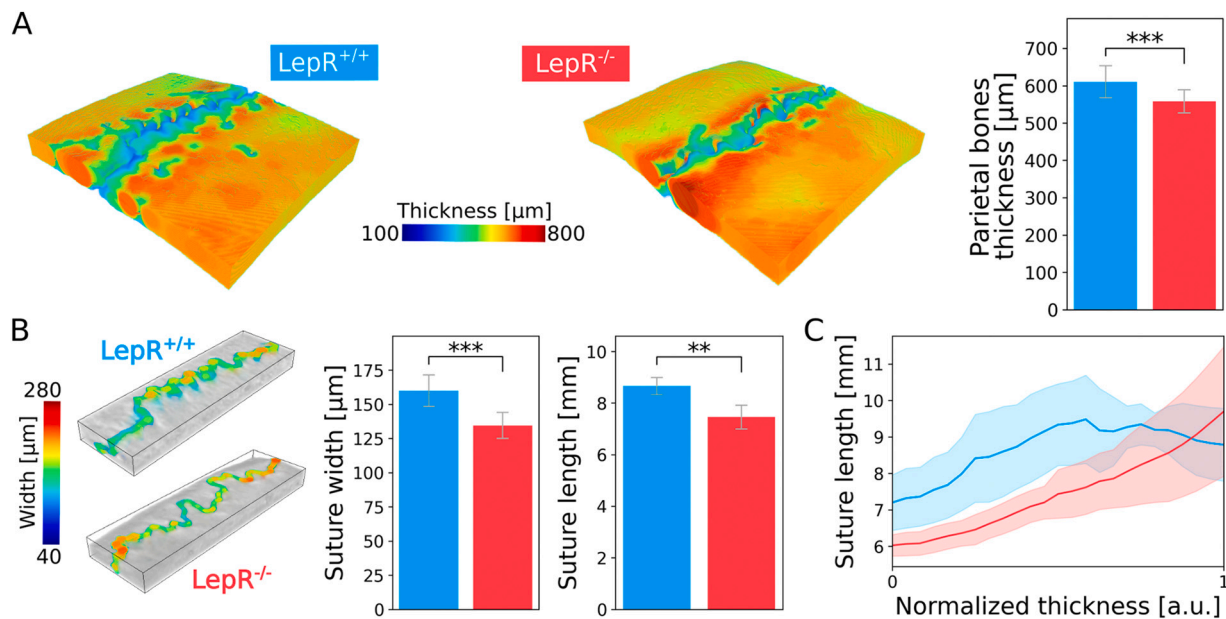
Fig. 4. Calvarium structure. A) Volume thickness map of parietal bones and relative bar plot, showing that the LepR^{-/-} animals (red bar) have significantly thinner parietal bones than the LepR^{+/+} animals (blue bar). B) 3D reconstruction of a representative section of parietal bones with the volume thickness map of the sagittal suture width, and bar plots summarizing the width and length of the sagittal suture. C) Variation in suture length along the calvarium thickness in the parietal region (normalized thickness is 0 towards the dura mater side and 1 towards the cranium exterior). The solid line corresponds to the average, while the faded region represents the standard deviation. ** and *** in the bar plots denote statistical significance ($p < 0.01$ and $p < 0.001$, respectively). (For interpretation of the references to colour in this figure legend, the reader is referred to the web version of this article.)

phenotype commonly identified in other rodent models of either hyperglycemia/T2DM, Lep/LepR deficiency, and obesity. Reduced bone length in femur and tibia [20,43,44] and altered morphological parameters (e.g., lower Ct.Th, Ct.Ar, BV/TV, Tb.Th, Tb.N; higher Tb.Sp) have been reported in both Zucker fatty and ZDF rats [44–46], consistently with what we observed in the LepR^{-/-} animals. Similar results have also been described in the mouse model equivalent to the Zucker fatty rat, the Lep[db/db] mouse [22], and in a LepR knockout rat developed using CRISPR/Cas9 technology [47]. The greater animal weight in the obese LepR^{-/-} animals also likely plays a role in the dissimilar bone shape and structure, since bone adapts to mechanical loads [48–50]. In particular, increased loading has been associated with reduced body growth and shorter tibia and femur [51]. However, this could be due to LepR deficiency only rather than greater loading due to weight, since leptin-independent regulation of body weight (i.e., the "gravitostat" [52]) has been challenged by studies in micro-gravity [53].

Macroscopically, calvaria were thinner in the parietal region of the LepR^{-/-} rats. In a rat model of streptozotocin (STZ)-induced DM, type 1 DM was also associated with smaller skulls, showing decreased cranial vault length and cranial base length in the neurocranium [54]. The smaller bone size in both calvaria and femurs, which also lacked full development in the femoral head and neck, suggests a delay in skeletal growth. A lower bone formation rate has also been reported in Lep[ob/ob] and Lep[db/db] mice compared to age-matched wild type controls [24]. The delayed skeletal growth also appears in agreement with the overall reduced development experienced by Lep/LepR-deficient humans [29–31].

To the best of our knowledge, suture morphology has never been studied in the context of LepR deficiency, diabetes, and obesity. However, sutures play an essential role in the development and morphology of the skull vault, acting as centres of intramembranous bone growth [55,56]. Considering that suture interdigitation increases with age [57], the shorter sagittal suture of the LepR^{-/-} animals further reinforces our hypothesis of delayed skeletal growth. Sutures usually display less interdigitation in the deeper side of the cranium, i.e., towards the dura mater [57]. Our observations on the variation in suture length, which is

representative of the degree of interdigitation, along the calvarium thickness confirm this trend. Interestingly, the suture length increases almost linearly across the calvarium thickness in the direction towards the cranium exterior in the LepR^{-/-} group, while it tends to plateau at around one third of the calvarium thickness in the LepR^{+/+} group. This could indicate that, while a sort of equilibrium in the development of suture morphology is reached in the LepR^{+/+} animals, substantial changes are still ongoing in the LepR^{-/-} rodents, given the higher variability in the degree of interdigitation.

The smaller width of the sagittal suture in the LepR^{-/-} animals appears in contrast with the hypothesis of reduced skeletal growth. Although in rodents the sagittal suture remain patent (unfused) throughout their lives [55], the sagittal suture narrows as the parietal bones thickens when the cranial expansion slows down [58,59]. Therefore, as skeletal growth is supposedly delayed in the LepR^{-/-} group, a wider, more patent suture would be expected. A reduction in sutural gap indicates an increased bone apposition at the suture edges operated by the osteoblasts, as bone remodeling has been identified as mechanism controlling suture patency [59]. Fat accumulation in obesity is usually thought to promote adipogenesis at the expense of osteoblastogenesis [10,11,60]. On the other hand, severe obesity appears to mitigate the skeletal changes in Lep[ob/ob] mice [61]. Lower bone formation rates have often been reported in Lep[ob/ob] and Lep[db/db] mice [24,62]. Obesity also appears to stimulate bone resorption thorough the RANK/RANKL pathway in presence of chronic inflammation [15]. Hence, one would expect bone resorption prevailing over bone formation in the LepR^{-/-} group, in turn leaving a wider suture. On the other hand, it is possible that the narrower sagittal suture reflects the lack of expansion of the cranial vault due to the delayed growth, resulting in the two parietal bones remaining closer to each other. Lastly, the width of the sagittal suture could simply be proportioned to the size of the calvaria, which is thinner in the parietal region of LepR^{-/-} animals, as it is known that skull and suture development are strongly linked [56,59]. It is also worth noting that sutures are very complex features to analyze, and, overall, there still is a lack of metrics to capture their complexity in a truly quantitative way [63].
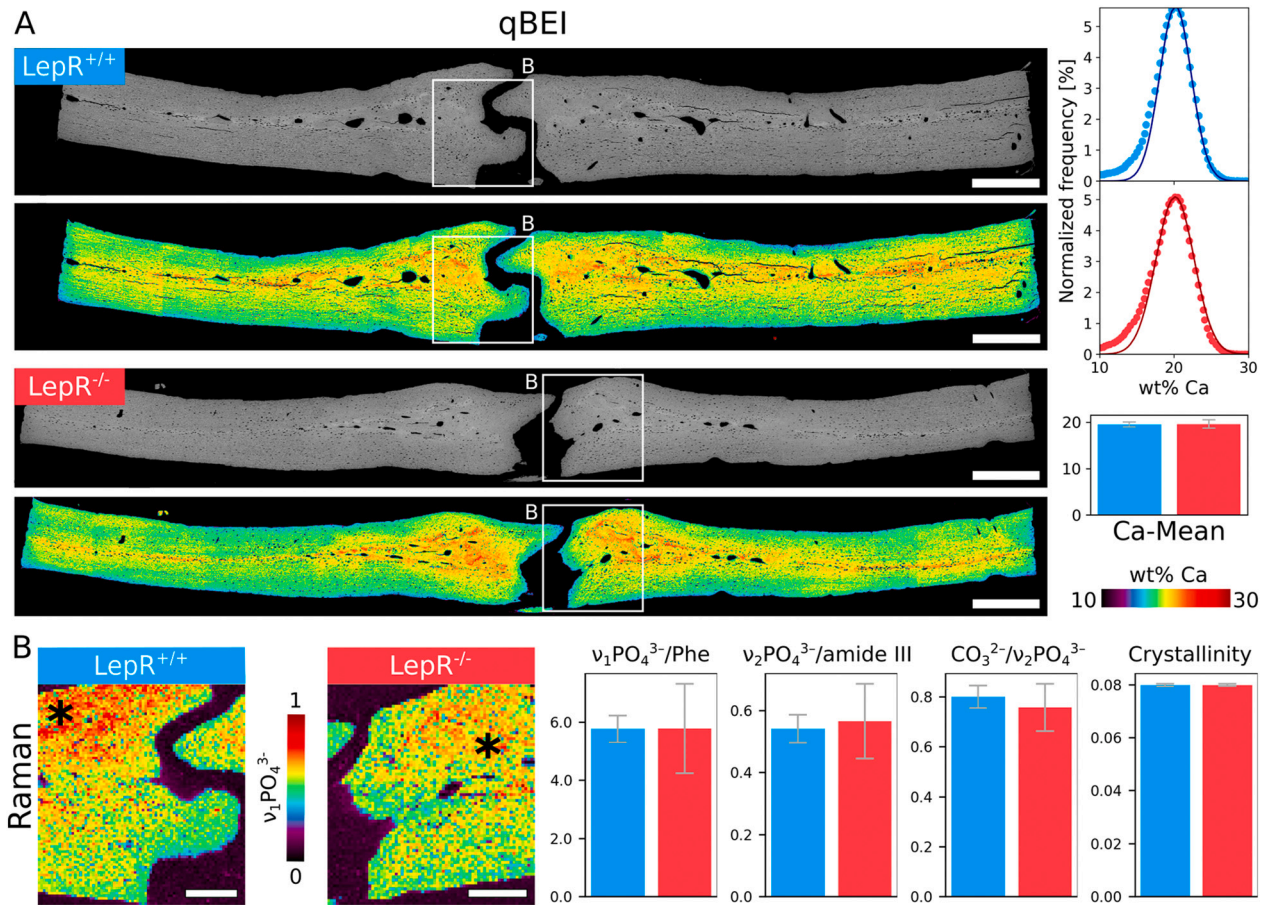
7

Fig. 5. Calvarium composition. A) Overview BSE-SEM image of cross-sections of representative calvaria (parietal region) of LepR$^{+/+}$ (colour-coded in blue) and LepR$^{-/-}$ animals (colour-coded in red), with corresponding qBEI images where pixel intensity corresponds to mineral concentration, expressed as wt% Ca, histograms (dots represent the histogram of the acquired data, and continuous line corresponds to the area-equivalent Gaussian curve) and bar plot for Ca-Mean. B) Raman maps (10 μm pixel size) of the $\nu_1 PO_4^{3-}$ peak intensity (normalized by the maximum value registered in the map), and bar plots summarizing the values of mineral-to-matrix ratio ($\nu_2 PO_4^{3-}$/amide III; $\nu_1 PO_4^{3-}$/Phe), carbonate-to-phosphate ratio ($CO_3^{2-}/\nu_2 PO_4^{3-}$), and mineral crystallinity (1/FWHM) measured in the maps. In the qBEI images and Raman maps, more mineralized regions (orange-to-red) can be noted. Some of these regions (* in the Raman maps) were examined at higher resolution (1 μm pixel size Raman maps, see Fig. 6). Scale bars are 500 μm in A and 200 μm in B. (For interpretation of the references to colour in this figure legend, the reader is referred to the web version of this article.)
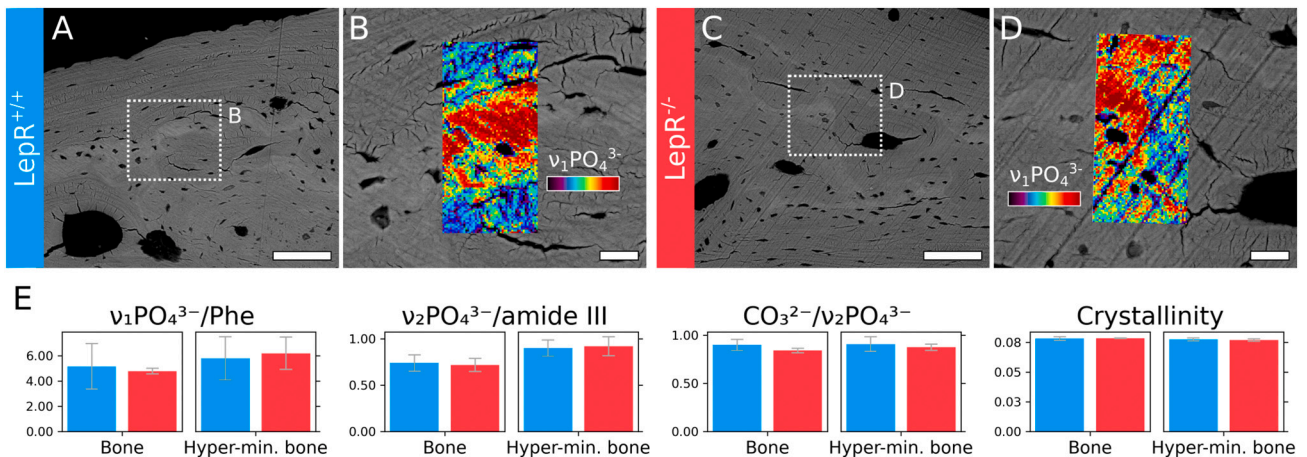

Fig. 6. Hyper-mineralized bone. A) Representative BSE-SEM image where areas of hyper-mineralized bone can be distinguished as the lighter grey regions within bone matrix (dark grey) in a LepR$^{+/+}$ animal. B) Higher magnification BSE-SEM image of the dotted region in A with superimposed Raman map (1 μm pixel size) of the $\nu_1 PO_4^{3-}$ peak intensity (restricted to 5–95% quantile range). C) Representative BSE-SEM image where areas of hyper-mineralized bone can be distinguished as the lighter grey regions within bone matrix (dark grey) in a LepR$^{-/-}$ animal. D) Higher magnification BSE-SEM image of the dotted region in C with superimposed Raman map (1 μm pixel size) of the $\nu_1 PO_4^{3-}$ peak intensity (restricted to 5–95% quantile range). E) Bar plots summarizing the values of mineral-to-matrix ratio ($\nu_2 PO_4^{3-}$/amide III; $\nu_1 PO_4^{3-}$/Phe), carbonate-to-phosphate ratio ($CO_3^{2-}/\nu_2 PO_4^{3-}$), and mineral crystallinity (1/FWHM) measured in bone and hyper-mineralized (Hyper-min.) bone in the Raman maps. Scale bars are 100 μm in A and C, and 20 μm in B and D.

4.2. Composition and mechanical properties

While microstructure presented substantial alterations in the LepR$^{-/-}$ animals, no significant differences in bone matrix composition were detected in neither femurs nor calvaria. All the different methods to assess composition used in this work confirmed this trend, regardless of the probe used to produce signals (X-rays in micro-CT; electron beam in qBEI; red-light laser in micro-Raman spectroscopy) and the resolution attainable (voxel size of 13.90–17.90 μm in micro-CT; pixel size around 1.3 μm in qBEI; pixel size of 1 μm and 10 μm in micro-Raman spectroscopy).

In a study by Creecy et al., Zucker Diabetic Sprague Dawley (ZDSD) rats displayed no significant differences in Ct.TMD and Tb.TMD in the femur compared to healthy Sprague Dawley rats at different ages (16, 22, and 29 weeks) [64]. Despite ZDSD rats have no LepR mutation [65], we found analogous results, with comparable values of TMD in both femoral cortical and trabecular bone and in the parietal bones of LepR$^{-/-}$ and LepR$^{+/+}$ animals. TMD is a metric for the degree of bone mineralization easily assessed in micro-CT systems, but it differs from the more widely used BMD parameter as TMD does not include the average attenuation from non-bone regions [36]. Patients with T2DM are commonly reported having normal or even higher values of BMD than non-diabetic individuals [11,12]. On the other hand, inconsistent trends in BMD have been observed in Zucker fa/fa rats, with values of BMD both comparable [45] or statistically reduced [21,43] with respect to healthy controls.

The absence of statistically significant differences in bone matrix mineralization expressed as TMD were corroborated by qBEI. In qBEI, the degree of mineralization of the bone matrix corresponds to the BMDD after proper calibration of grey-levels in BSE-SEM images using standards of C and Al [38]. This method was developed by Roschger et al. to mitigate the limitations of BMD measures, where changes in bone volume cannot be differentiated from those in bone matrix mineralization [38]. In our BSE-SEM images acquired post-calibration, no differences in BMDD between LepR$^{-/-}$ and LepR$^{+/+}$ rats were detected in neither femurs nor calvaria. Comparable BMDD was also found between 21-week-old ZDF and non-diabetic rats in qBEI carried out by Hamann et al., where differences were only observed in the femur metaphysis, but not in the epiphysis nor in the cortical mid-shaft [66].

In agreement with TMD and BMDD evaluated by micro-CT and qBEI, respectively, differences in values of mineral-to-matrix ratio assessed micro-Raman spectroscopy were not statistically significant in neither femurs (cortical and trabecular bone) nor calvaria, regardless of the bands considered ($\nu_2 PO_4^{3-}$/amide III; $\nu_1 PO_4^{3-}$/Phe). This is not surprising, as a strong correlation between $\nu_2 PO_4^{3-}$/amide III in micro-Raman spectroscopy and wt% Ca in qBEI has been demonstrated [67]. In the Raman maps with a 10 μm pixel size, the trend of lower mineral-to-matrix ratio in the femurs of LepR$^{-/-}$ animals, indicating reduced mineralization, appeared in agreement with the delayed growth suggested by the altered microarchitecture. However, clear conclusions cannot be drawn, given the absence of statistical significance and the lack of a similar trend in the Raman maps with a 1 μm pixel size. Moreover, carbonate-to-phosphate ratio, which normally increases with tissue age [42,68], and mineral crystallinity were comparable in both animal groups, further suggesting no differences in the degree of skeletal maturity in terms of bone matrix composition. Other authors have reported a similar lack of variation in bone composition (mineral-to-matrix ratio and carbonate substitution) in trabecular bone in the peri-implant space of ZDF and Sprague Dawley rats [69]. Hammond et al. also reported comparable values of carbonate-to-phosphate ratio and mineral crystallinity in ZDSD and Sprague Dawley rats [70]. On the other hand, they found that mineral-to-matrix ratio was higher in the ZDSD animals [70]. However, this discrepancy can be attributed to the different bands used to compute the mineral-to-matrix ratio in the Raman spectra. In a recent study by Monahan et al., Fourier transform infrared (FTIR) spectroscopy revealed comparable mineral-to-matrix

ratio and mineral crystallinity in ZDF and control rats at all ages examined (12, 26, and 46 weeks of age), while acid phosphate content and carbonate-to-phosphate ratio showed statistically significant differences in 46-week-old animals (with acid phosphate being different also at 12 weeks) [71].

Parameters related to mechanical properties evaluated by RPI were comparable in the femurs of LepR$^{+/+}$ and LepR$^{-/-}$ rats. In a previous study, Hammond et al. found statistically significant differences in CID 1st and IDI, which the authors concluded to be caused by increased resistance to plastic deformation and reduced fracture toughness due to AGEs crosslinking [70]. Here, the comparable RPI measurements are consistent with the similarity in bone matrix composition. Although microstructural differences are expected to impact mechanical properties, these are likely not captured by RPI, as fracture risk is also determined by trabecular and intracortical properties, which are not assessed by periosteal indentation [72].

4.3. Notable microstructural features

Part of our analyses focused on some specific microstructural features noted in BSE-SEM images, in particular, mineralized cartilage islands in the femurs and more highly mineralized bone areas in the calvaria. Mineralized cartilage islands have been reported in the femoral cortical bone of both mice [73] and rats [39,74]. As these islands are observed also in skeletally mature animals, and not just in those at growing stages, they are believed to be remnants of endochondral ossification due to the little to no Haversian remodeling in rodents [39,74]. Where Haversian remodeling takes place, such as in human bone, mineralized cartilage is not present as islands enclosed by bone, but it is mostly noted at subchondral bone-cartilage interfaces at the growth plates or at the joints [75,76], and in the femoral neck of elderly subjects [77].

Here, mineralized cartilage islands were observed also in the trabecular region, further confirming mineralized cartilage as a characteristic feature of rodent bone, regardless of the type (cortical vs. trabecular). These elements could be easily distinguished from the surrounding bone matrix as they presented a higher degree of mineralization, i.e., they appeared considerably brighter in BSE-SEM images. High-resolution Raman maps (1 μm pixel size) also confirmed the higher mineral content of mineralized cartilage islands compared to bone in both cortical and trabecular regions. This trend was consistent in both LepR$^{-/-}$ and LepR$^{+/+}$ animals, although differences were not statistically significant. A higher sample number could be probed to verify whether the lack of statistical differences corresponds to a true lack of difference, or whether the study is underpowered. In fact, previous work reported a significantly higher degree of mineralization in mineralized cartilage islands than in bone using qBEI [39]. In our work, qBEI was completed to gain global information on the degree of mineralization over large sample areas, hence the magnification and standard used were not suitable to exactly probe compositional differences between mineralized cartilage islands and bone. Nonetheless, we analyzed our qBEI data by dividing them in 5 wt% Ca-wide bins to assess eventual differences in the amount of mineralized cartilage islands in LepR$^{-/-}$ and LepR$^{+/+}$ animals, assuming this would be reflected by a greater pixel count in the bins corresponding to high values of wt% Ca. However, no differences between groups were found. This was expected, as drastic differences in mineralized cartilage islands content would have altered the overall degree of mineralization of bone matrix, which was indeed comparable in the two animal groups for all the compositional analyses completed (TMD by micro-CT, BMDD by qBEI, and mineral-to-matrix ratio by micro-Raman spectroscopy).

In analogy with the mineralized cartilage islands indicating partial remodeling in endochondral bones, we hypothesize that hyper-mineralized bone in the calvaria is also related to incomplete/ongoing remodeling. From qBEI images and Raman maps (10 μm pixel size), it appears that bone is less mineralized at its surfaces (superior, inferior,

and suture edge). Therefore, it is possible that hyper-mineralized bone corresponds to older, more mineralized bone that will progressively be replaced by new tissue as remodeling takes place. LepR$^{-/-}$ animals had a similar content of hyper-mineralized bone as the LepR$^{+/+}$ group when comparing different 5 wt% Ca bins in qBEI data. This further confirms the comparable bone matrix composition in the two groups examined, regardless of the anatomical location (femur vs. calvarium).

4.4. Limitations and future directions

To the best of our knowledge, this is the first examination of Lund MetS rats addressing skeletal changes, as previous work investigated vasculature complications [32–34]. While the focus of the present study is on microstructure and bone matrix composition, more work is needed to comprehensively characterize the skeletal phenotype of Lund MetS rats, which is especially important in order to establish whether they can constitute a valid alternative to already available LepR-deficient rodent models for diabetes research.

Presently, it is not possible to establish whether the skeletal abnormalities in the Lepr$^{-/-}$ group are due to LepR deficiency, obesity, hyperglycemia, or a combination thereof. While decoupling these variables was out-of-scope in this work, such a task was accomplished in previous studies for example by pair-feeding [61] or bone marrow transplantation [24]. Hence, a similar methodological approach could be applied in the future to gain mechanistic insights on the altered microstructure and reduced bone mass in the trabecular compartment of the Lund MetS rats.

The role of AGEs accumulation in increasing fracture risk has often been emphasized in diabetic individuals. Interestingly, a recent study showed no correlation between mechanical properties and AGEs in ZDF rats [71], while others have observed an increased resistance to indentation in ZDSD animals, which, combined with an altered collagen D-spacing, corroborates the direct effect of AGEs on the mechanical behaviour of collagen fibrils [70]. The amount of AGEs and the eventual correlation with mechanical properties should also be assessed in the Lund MetS rats. The analysis should not be limited to more commonly measured fluorescent AGEs like PEN, but also include non-fluorescent, non-crosslinking AGEs like CML, which is found in greater content than PEN in human cortical bone [78].

Here, insights into mechanical properties were partially gained from indentation-related response through RPI. However, geometrical and microstructural alterations in the femurs of LepR$^{-/-}$ animals are likely to cause an abnormal mechanical behaviour not detected by RPI via periosteal measurements, which we believe to be more influenced by bone matrix composition. Mechanical testing of whole bones with a three-point bend test would be a more fitting approach to confirm loss in bone strength and toughness induced by microstructural alterations.

The similarity in bone matrix composition and features related to remodeling (mineralized cartilage islands and hyper-mineralized bone in femurs and calvaria, respectively) are indicative of comparable bone turnover in the two groups. On the other hand, previous studies showed higher content of mineralized cartilage and lower bone turnover in Lep$^{ob/ob}$ and Lep$^{db/db}$ mice [24,62]. Static and dynamic histomorphometry and evaluation of bone formation/resorption markers (e.g., through serum analysis) are therefore necessary to eventually confirm the differences in bone turnover between LepR$^{-/-}$ and LepR$^{+/+}$ animals. This will also have relevant implications for bone repair and regeneration, for example in the context of osseointegration. Although osseointegration outcomes in patients with T2DM under glycemic control are generally positive, chronic hyperglycemia impairs wound healing, potentially leading to implant failure [79].

Fracture risk in diabetic subjects appears to be correlated with disease duration [80]. As bone strength was shown to worsen with disease progression in ZDF rats [71], a longitudinal study of Lund MetS rats would offer insights into the time-evolution of the skeletal alterations in the LepR$^{-/-}$ animals and their impact on mechanical properties. Lastly,

while only male rats were used in this study, female rats should also be investigated in the future. Lund MetS LepR$^{-/-}$ female rats display impaired glucose tolerance and obesity, but do not develop overt T2DM [32,35], similarly to ZDF rats [16]. Nonetheless, given the incidence of obesity in both sexes, together with reports of LepR-deficiency in female individuals [30], such an animal model can still be employed in contexts relevant to human research.

5. Conclusion

Regardless of the ossification route, the LepR$^{-/-}$ animals presented altered morphology and microarchitecture in both femurs and calvaria. On the other hand, bone matrix composition was comparable to that of the control group. Similarly, specific microstructural features like mineralized cartilage islands in the femurs and hyper-mineralized bone in the calvaria also appeared equally distributed in the two groups. Therefore, it seems that the altered metabolic state in the LepR$^{-/-}$ animals affects bone formation macroscopically (e.g., shorter femurs, thinner calvaria) and microscopically (e.g., more porous trabecular region, shorter sagittal suture), leading to a delayed skeletal development. In spite of the analogous composition and RPI measurements, LepR$^{-/-}$ animals are expected to display impaired mechanical functions, given the compromised macro- and microstructure. Overall, our findings are consistent with the delayed development experienced by humans with Lep/LepR congenic mutations [29–31], and with the altered bone microstructure of diabetic subjects [11], making this animal model promising for translational bone research.

CRediT authorship contribution statement

Chiara Micheletti: Conceptualization, Methodology, Formal analysis, Investigation, Visualization, Writing – original draft. **Martina Jolic:** Investigation, Writing – review & editing. **Kathryn Grandfield:** Supervision, Funding acquisition, Writing – review & editing. **Furqan A. Shah:** Conceptualization, Methodology, Investigation, Supervision, Funding acquisition, Writing – review & editing. **Anders Palmquist:** Conceptualization, Methodology, Investigation, Supervision, Funding acquisition, Writing – review & editing.

Declaration of competing interest

The authors declare that they have no known competing financial interests or personal relationships that could have appeared to influence the work reported in this paper.

Data availability

Additional data are available in Supplementary Material.

Acknowledgements

Research Council (grant no. 2020-04715), the Swedish state under the agreement between the Swedish government and the county councils, the ALF agreement (ALFGBG-725641), the IngaBritt and Arne Lundberg Foundation, the Hjalmar Svensson Foundation, and the Area of Advance Materials at Chalmers and at the Department of Biomaterials (University of Gothenburg) within the Strategic Research Area initiative launched by the Swedish government.

Appendix A. Supplementary data

Supplementary data to this article can be found online at https://doi.org/10.1016/j.bone.2023.116747.

References

[1] G.J. Tortora, B. Derrickson, The skeletal system: bone tissue, in: Principles of Anatomy and Physiology, John Wiley & Sons, New York NY, 2009.

[2] M.R. Allen, D.B. Burr, Bone modeling and remodeling, in: Basic and Applied Bone Biology, Academic Press, London, UK, 2014, pp. 75–90.

[3] G.L. Galea, M.R. Zein, S. Allen, P. Francis-West, Making and shaping endochondral and intramembranous bones, Dev. Dyn. 250 (2021) 414–449.

[4] N. Reznikov, R. Shahar, S. Weiner, Bone hierarchical structure in three dimensions, Acta Biomater. 10 (2014) 3815–3826.

[5] M.L. Bouxsein, Bone quality: where do we go from here? Osteoporos. Int. 14 (2003) 118–127.

[6] A.L. Boskey, L. Imbert, Bone quality changes associated with aging and disease: a review, Ann. N. Y. Acad. Sci. 1410 (2017) 93–106.

[7] A. Muñoz, A. Docaj, M. Ugarteburu, A. Carriero, Poor bone matrix quality: what can be done about it? Curr. Osteoporos. Rep. 19 (2021) 510–531.

[8] L.R. McCabe, The diabetes-bone relationship, J. Diabetes Metab. 3 (2012), e001.

[9] W.D. Leslie, M.R. Rubin, A.V. Schwartz, J.A. Kanis, Type 2 diabetes and bone, J. Bone Miner. Res. 27 (2012) 2231–2237.

[10] J.J. Cao, Effects of obesity on bone metabolism, J. Orthop. Surg. Res. 6 (2011) 30.

[11] L. McCabe, J. Zhang, S. Raehtz, Understanding the skeletal pathology of type 1 and 2 diabetes mellitus, Crit. Rev. Eukaryot. Gene Expr. 21 (2011) 187–206.

[12] L.J. Melton, B.L. Riggs, C.L. Leibson, S.J. Achenbach, J.J. Camp, M.L. Bouxsein, E. J. Atkinson, R.A. Robb, S. Khosla, A bone structural basis for fracture risk in diabetes, J. Clin. Endocrinol. Metab. 93 (2008) 4804–4809.

[13] M. Yamamoto, T. Sugimoto, Advanced glycation end products, diabetes, and bone strength, Curr. Osteoporos. Rep. 14 (2016) 320–326.

[14] M. Saito, Y. Kida, S. Kato, K. Marumo, Diabetes, collagen, and bone quality, Curr. Osteoporos. Rep. 12 (2014) 181–188.

[15] G.V. Halade, A.E. Jamali, P.J. Williams, R.J. Fajardo, G. Fernandes, Obesity-mediated inflammatory microenvironment stimulates osteoclastogenesis and bone loss in mice, Exp. Gerontol. 46 (2011) 43–52.

[16] A.J. King, The use of animal models in diabetes research, Br. J. Pharmacol. 166 (2012) 877–894.

[17] L.A. Tartaglia, The leptin receptor, J. Biol. Chem. 272 (1997) 6093–6096.

[18] I.R. Reid, P.A. Baldock, J. Cornish, Effects of leptin on the skeleton, Endocr. Rev. 39 (2018) 938–959.

[19] J. Cornish, K. Callon, U. Bava, C. Lin, D. Naot, B. Hill, A. Grey, N. Broom, D. Myers, G. Nicholson, I. Reid, Leptin directly regulates bone cell function in vitro and reduces bone fragility in vivo, J. Endocrinol. 175 (2002) 405–415.

[20] J. Foldes, M.S. Shih, J. Levy, Bone structure and calcium metabolism in obese zucker rats, Int. J. Obes. Relat. Metab. Disord. 16 (1992) 95–102.

[21] J. Mathey, M.-N. Horcajada-Molteni, B. Chanteranne, C. Picherit, C. Puel, P. Lebecque, C. Cubizoles, M.-J. Davicco, V. Coxam, J.-P. Barlet, Bone mass in obese diabetic zucker rats: influence of treadmill running, Calcif. Tissue Int. 70 (2002) 305–311.

[22] G.A. Williams, K.E. Callon, M. Watson, J.L. Costa, Y. Ding, M. Dickinson, Y. Wang, D. Naot, I.R. Reid, J. Cornish, Skeletal phenotype of the leptin receptor–deficient db/db mouse, J. Bone Miner. Res. 26 (2011) 1698–1709.

[23] P. Ducy, M. Amling, S. Takeda, M. Priemel, A.F. Schilling, F.T. Beil, J. Shen, C. Vinson, J.M. Rueger, G. Karsenty, Leptin inhibits bone formation through a hypothalamic relay a central control of bone mass, Cell 100 (2000) 197–207.

[24] R.T. Turner, S.P. Kalra, C.P. Wong, K.A. Philbrick, L.B. Lindenmaier, S. Boghossian, U.T. Iwaniec, Peripheral leptin regulates bone formation, J. Bone Miner. Res. 28 (2013) 22–34.

[25] B. Burguera, L.C. Hofbauer, T. Thomas, F. Gori, G.L. Evans, S. Khosla, B.L. Riggs, R. T. Turner, Leptin reduces ovariectomy-induced bone loss in rats, Endocrinology 142 (2001) 3546–3553.

[26] S.M. Bartell, S. Rayalam, S. Ambati, D.R. Gaddam, D.L. Hartzell, M. Hamrick, J. She, M.A. Della-Fera, C.A. Baile, Central (ICV) leptin injection increases bone formation, bone mineral density, muscle mass, serum IGF-1, and the expression of osteogenic genes in leptin-deficient ob/ob mice, J. Bone Miner. Res. 26 (2011) 1710–1720.

[27] B. Wang, P. Chandrasekera, J. Pippin, Leptin- and leptin receptor-deficient rodent models: relevance for human type 2 diabetes, Curr. Diabetes Rev. 10 (2014) 131–145.

[28] C.T. Montague, I.S. Farooqi, J.P. Whitehead, M.A. Soos, H. Rau, N.J. Wareham, C. P. Sewter, J.E. Digby, S.N. Mohammed, J.A. Hurst, C.H. Cheetham, A.R. Earley, A.

[29] H. Barnett, J.B. Prins, S. O'Rahilly, Congenital leptin deficiency is associated with severe early-onset obesity in humans, Nature 387 (1997) 903–908.

[30] K. Clément, C. Vaisse, N. Lahlou, S. Cabrol, V. Pelloux, D. Cassuto, M. Gourmelen, C. Dina, J. Chambaz, J.-M. Lacorte, A. Basdevant, P. Bougnères, Y. Lebouc, P. Froguel, B. Guy-Grand, A mutation in the human leptin receptor gene causes obesity and pituitary dysfunction, Nature 392 (1998) 398–401.

[31] I.S. Farooqi, T. Wangensteen, S. Collins, W. Kimber, G. Matarese, J.M. Keogh, E. Lank, B. Bottomley, J. Lopez-Fernandez, I. Ferraz-Amaro, M.T. Dattani, O. Ercan, A.G. Myhre, L. Retterstol, R. Stanhope, J.A. Edge, S. McKenzie, N. Lessan, M. Ghodsi, V.D. Rosa, F. Perna, S. Fontana, I. Barroso, D.E. Undlien, S. O'Rahilly, Clinical and molecular genetic Spectrum of congenital deficiency of the leptin receptor, N. Engl. J. Med. 356 (2007) 237–247.

[31] I.S. Farooqi, S. O'Rahilly, 20 years of leptin: human disorders of leptin action, J. Endocrinol. 223 (2014) T63–T70.

[32] M.F. Gomez , L. Åkesson, Å. Lernmark, A new rat model for diabetic vascular complications, Patent Application WO-2015044339-A1.

[33] M.F. Gomez, J. Silvola, L.M. Berglund, L. Kiugel, L. Åkesson, J. Knuuti, A. Roivainen, Å. Lernmark, P. Nuutila, A. Saraste, Cardiac hypertrophy and oxidative metabolism in novel congenic leptin receptor deficient BBDR.Cg-lepr.Cp rats, FASEB J. 28 (2014), 1155.10.

[34] L. Berglund, L. Åkesson, E.G. Vaz, A. Zetterqvist, O. Kotova, A.D. Andersson, M. Johansson, N. Wierup, A. Jönsson-Rylander, Å. Lernmark, M. Gomez, Diabetes complications in congenic leptin receptor deficient BBDR.Cg-lepr.Cp rats, FASEB J. 28 (2014), 1072.6.

[35] Janvier Labs, Lund MetS rat. https://janvier-labs.com/en/fiche_produit/lund-mets_rat/.

[36] M.L. Bouxsein, S.K. Boyd, B.A. Christiansen, R.E. Guldberg, K.J. Jepsen, R. Müller, Guidelines for assessment of bone microstructure in rodents using micro–computed tomography, J. Bone Miner. Res. 25 (2010) 1468–1486.

[37] H.R. Buie, G.M. Campbell, R.J. Klinck, J.A. MacNeil, S.K. Boyd, Automatic segmentation of cortical and trabecular compartments based on a dual threshold technique for in vivo micro-CT bone analysis, Bone 41 (2007) 505–515.

[38] P. Roschger, P. Fratzl, J. Eschberger, K. Klaushofer, Validation of quantitative backscattered electron imaging for the measurement of mineral density distribution in human bone biopsies, Bone 23 (1998) 319–326.

[39] F.L. Bach-Gansmo, S.C. Irvine, A. Brüel, J.S. Thomsen, H. Birkedal, Calcified cartilage islands in rat cortical bone, Calcif. Tissue Int. 92 (2013) 330–338.

[40] S. Gamsjaeger, A. Masic, P. Roschger, M. Kazanci, J.W.C. Dunlop, K. Klaushofer, E. P. Paschalis, P. Fratzl, Cortical bone composition and orientation as a function of animal and tissue age in mice by raman spectroscopy, Bone 47 (2010) 392–399.

[41] J.P. McElderry, G. Zhao, A. Khmaladze, C.G. Wilson, R.T. Franceschi, M.D. Morris, Tracking circadian rhythms of bone mineral deposition in murine calvarial organ cultures, J. Bone Miner. Res. 28 (2013) 1846–1854.

[42] M.D. Morris, G.S. Mandair, Raman assessment of bone quality, Clin. Orthop. Relat. Res. 469 (2011) 2160–2169.

[43] R.D. Prisby, J.M. Swift, S.A. Bloomfield, H.A. Hogan, M.D. Delp, Altered bone mass, geometry and mechanical properties during the development and progression of type 2 diabetes in the zucker diabetic fatty rat, J. Endocrinol. 199 (2008) 379–388.

[44] S. Reinwald, R.G. Peterson, M.R. Allen, D.B. Burr, Skeletal changes associated with the onset of type 2 diabetes in the ZDF and ZDSD rodent models, Am. J. Physiol. Endocrinol. Metab. 296 (2009) E765–E774.

[45] J.A. Tamasi, B.J. Arey, D.R. Bertolini, J.H. Feyen, Characterization of bone structure in leptin receptor-deficient zucker (fa/fa) rats, J. Bone Miner. Res. 18 (2003) 1605–1611.

[46] D. Zeitoun, G. Caliaperoumal, M. Bensidhoum, J.M. Constans, F. Anagnostou, V. Bousson, Microcomputed tomography of the femur of diabetic rats: alterations of trabecular and cortical bone microarchitecture and vasculature—a feasibility study, Eur. Radiol. Exp. 3 (2019) 17.

[47] D. Bao, Y. Ma, X. Zhang, F. Guan, W. Chen, K. Gao, C. Qin, L. Zhang, Preliminary characterization of a leptin receptor knockout rat created by CRISPR/Cas9 system, Sci. Rep. 5 (2015) 15942.

[48] J.D. Wolff, The Law of Bone Transformation, Hirschwald, Berlin, 1892.

[49] J.D. Currey, Bones: Structure and Mechanics, Princeton University Press, Princeton NJ, 2002.

[50] A.G. Robling, C.H. Turner, Mechanical signaling for bone modeling and remodeling, Crit. Rev. Eukaryot. Gene Expr. 19 (2009) 319–338.

[51] J.-O. Jansson, A.D. Gasull, E. Schéle, S.L. Dickson, V. Palsdottir, A. Palmquist, F. F. Gironés, J. Bellman, F. Anesten, D. Hägg, C. Ohlsson, A body weight sensor regulates pre-pubertal growth via the somatotropic axis in male rats, Endocrinology 162 (2021) bqab053-.

[52] J.-O. Jansson, V. Palsdottir, D.A. Hägg, E. Schéle, S.L. Dickson, F. Anesten, T. Bake, M. Montelius, J. Bellman, M.E. Johansson, R.D. Cone, D.J. Drucker, J. Wu, B. Aleksic, A.E. Törnqvist, K. Sjögren, J.-Å. Gustafsson, S.H. Windahl, C. Ohlsson, Body weight homeostat that regulates fat mass independently of leptin in rats and mice, Proc. Natl. Acad. Sci. 115 (2018) 427–432.

[53] R.T. Turner, A.J. Branscum, C.P. Wong, U.T. Iwaniec, E. Morey-Holton, Studies in microgravity, simulated microgravity and gravity do not support a gravitostat, J. Endocrinol. 247 (2020) 273–282.

[54] M.A. Abbassy, I. Watari, K. Soma, Effect of experimental diabetes on craniofacial growth in rats, Arch. Oral Biol. 53 (2008) 819–825.

[55] L.A. Opperman, Cranial sutures as intramembranous bone growth sites, Dev. Dyn. 219 (2000) 472–485.

[56] K.A. Lenton, R.P. Nacamuli, D.C. Wan, J.A. Helms, M.T. Longaker, Cranial suture biology, Curr. Top. Dev. Biol. 66 (2005) 287–328.

[57] T. Miura, C.A. Perlyn, M. Kinboshi, N. Ogihara, M. Kobayashi-Miura, G.M. Morriss-Kay, K. Shiota, Mechanism of skull suture maintenance and interdigitation, J. Anat. 215 (2009) 642–655.

[58] B. Zimmermann, A. Moegelin, P. de Souza, J. Bier, Morphology of the development of the sagittal suture of mice, Anat. Embryol. 197 (1998) 155–165.

[59] H.E. White, A. Goswami, A.S. Tucker, The intertwined evolution and development of sutures and cranial morphology, Front. Cell Dev. Biol. 09 (2021), 653579.

[60] Y. Hamada, H. Fujii, M. Fukagawa, Role of oxidative stress in diabetic bone disorder, Bone 45 (2009) S35–S38.

[61] R.T. Turner, K.A. Philbrick, C.P. Wong, D.A. Olson, A.J. Branscum, U.T. Iwaniec, Morbid obesity attenuates the skeletal abnormalities associated with leptin deficiency in mice, J. Endocrinol. 223 (2014) M1–M15.

[62] K.A. Philbrick, S.A. Martin, A.R. Colagiovanni, A.J. Branscum, R.T. Turner, U.T. Iwaniec, Effects of hypothalamic leptin gene therapy on osteopetrosis in leptin-deficient mice, J. Endocrinol. 236 (2018) 57–68.

[63] H.E. White, J. Clavel, A.S. Tucker, A. Goswami, A comparison of metrics for quantifying cranial suture complexity, J. R. Soc. Interface 17 (2020), 20200476.

[64] A. Creecy, S. Uppuganti, A.R. Merkel, D. O'Neal, A.J. Makowski, M. Granke, P. Voziyan, J.S. Nyman, Changes in the fracture resistance of bone with the progression of type 2 diabetes in the ZDSD rat, Calcif. Tissue Int. 99 (2016) 289–301.

[65] A.N. Wang, J. Carlos, G.M. Fraser, J.J. McGuire, Zucker diabetic-Sprague dawley (ZDSD) rat: type 2 diabetes translational research model, Exp. Physiol. 107 (2022) 265–282.

[66] C. Hamann, C. Goettsch, J. Mettelsiefen, V. Henkenjohann, M. Rauner, U. Hempel, R. Bernhardt, N. Fratzl-Zelman, P. Roschger, S. Rammelt, K.-P. Günther, L.C. Hofbauer, Delayed bone regeneration and low bone mass in a rat model of insulin-resistant type 2 diabetes mellitus is due to impaired osteoblast function, Am. J. Physiol. Endocrinol. Metab. 301 (2011) E1220–E1228.

[67] A. Roschger, S. Gamsjaeger, B. Hofstetter, A. Masic, S. Blouin, P. Messmer, A. Berzlanovich, E.P. Paschalis, P. Roschger, K. Klaushofer, P. Fratzl, Relationship between the v2PO4/amide III ratio assessed by raman spectroscopy and the calcium content measured by quantitative backscattered electron microscopy in healthy human osteonal bone, J. Biomed. Opt. 19 (2014), 065002-065002.

[68] D.B. Burr, Changes in bone matrix properties with aging, Bone 120 (2019) 85–93.

[69] K.D. Anderson, F.C. Ko, S. Fullam, A.S. Virdi, M.A. Wimmer, D.R. Sumner, R.D. Ross, The relative contribution of bone microarchitecture and matrix composition to implant fixation strength in rats, J. Orthop. Res. 40 (2022) 862–870.

[70] M.A. Hammond, M.A. Gallant, D.B. Burr, J.M. Wallace, Nanoscale changes in collagen are reflected in physical and mechanical properties of bone at the microscale in diabetic rats, Bone 60 (2014) 26–32.

[71] G.E. Monahan, J. Schiavi-Tritz, M. Britton, T.J. Vaughan, Longitudinal alterations in bone morphometry, mechanical integrity and composition in Type-2 diabetes in a zucker diabetic fatty (ZDF) rat, Bone 170 (2023), 116672.

[72] M.R. Allen, E.M. McNerny, J.M. Organ, J.M. Wallace, True gold or pyrite: a review of reference point indentation for assessing bone mechanical properties in vivo, J. Bone Miner. Res. 30 (2015) 1539–1550.

[73] V. Ip, Z. Toth, J. Chibnall, S. McBride-Gagyi, Remnant woven bone and calcified cartilage in mouse bone: differences between Ages/Sex and effects on bone strength, PLoS One 11 (2016), e0166476.

[74] A. Shipov, P. Zaslansky, H. Riesemeier, G. Segev, A. Atkins, R. Shahar, Unremodeled endochondral bone is a major architectural component of the cortical bone of the rat (Rattus norvegicus), J. Struct. Biol. 183 (2013) 132–140.

[75] T.R. Oegema, R.J. Carpenter, F. Hofmeister, R.C. Thompson, The interaction of the zone of calcified cartilage and subchondral bone in osteoarthritis, Microsc. Res. Tech. 37 (1997) 324–332.

[76] Y. Zhang, F. Wang, H. Tan, G. Chen, L. Guo, L. Yang, Analysis of the mineral composition of the human calcified cartilage zone, Int. J. Med. Sci. 9 (2012) 353–360.

[77] T. Tang, W. Wagermaier, R. Schuetz, Q. Wang, F. Eltit, P. Fratzl, R. Wang, Hypermineralization in the femoral neck of the elderly, Acta Biomater. 89 (2019) 330–342.

[78] C.J. Thomas, T.P. Cleland, G.E. Sroga, D. Vashishth, Accumulation of carboxymethyl-lysine (CML) in human cortical bone, Bone 110 (2018) 128–133.

[79] F. Javed, G.E. Romanos, Chronic hyperglycemia as a risk factor in implant therapy, Periodontol. 2000 (81) (2019) 57–63.

[80] A.D. Dede, S. Tournis, I. Dontas, G. Trovas, Type 2 diabetes mellitus and fracture risk, Metabolis. 63 (2014) 1480–1490.